Hotspots of acceleration and demographic processes behind decline of North American birds

François Leroy [1,2], Marta A. Jarzyna [2,3], Petr Keil [1]*

[1]*Department of Spatial Sciences, Faculty of Environmental Sciences, Czech University of Life Sciences Prague, Kamýcká 129, 16500 Praha-Suchdol, Czech Republic*

[2] *Department of Evolution, Ecology and Organismal Biology, The Ohio State University, Columbus, Ohio, 43210, USA*

[3] *Translational Data Analytics Institute, The Ohio State University, Columbus, Ohio, 43210, USA*

[*] *Correspondence:* leroy@fzp.czu.cz

Abstract

Human activities might have accelerated declines of population abundances, but this acceleration remains underexplored. Using the North American Breeding Bird Survey, we analyze abundance changes, acceleration, and demographic processes of recruitment and loss across 234 bird species from 1987 to 2021. We show a continent-wide decline of bird abundance, with hotspots of acceleration in the Mid-Atlantic, Midwest, and California, matching patterns of agricultural activities. In California and the Midwest, increasing loss rates drive acceleration, while in the Mid-Atlantic, declining recruitment is the main process behind the acceleration. Notably, 67% of increasing species and 95% of increasing families show declining recruitment rates, underscoring the need for conservation policies that enhance recruitment, not just prevent loss, even for seemingly thriving species.

Main text

Human activities such as changes in land-use, agricultural intensification, overexploitation, and pollution have significantly impacted ecosystems over the past centuries [IPBES (*1*)]. Temporal changes in local population abundances are a closely monitored indicator of this impact (*2*), and have shown an overall decline of abundances across taxa (*1*, *3*). The past century, however, has seen not only the increase but also an acceleration of the increase of human activities, sometimes termed the Great Acceleration (*4*–*6*), and a likely acceleration of global vertebrate extinction rates (*7*–*9*). We should thus expect a corresponding acceleration in population declines. In essence, while the first order derivative of population abundance change for many species appears to be a decline, the second order derivative (*i.e.* acceleration or deceleration of this change) has so far only been used to detect year-specific shifts in population trajectories (*10*–*12*).

While examining the temporal changes in population abundance is valuable, understanding the underlying demographic processes (such as recruitment and loss) can offer deeper ecological insights into the mechanisms of population dynamics. Change in abundance over time, ΔN, arises from the difference between recruitment R (*i.e.* number of new individuals entering the population through birth or immigration, Fig. 1A) and loss L (*i.e.* number of individuals removed from the population by death or emigration). The yearly growth rate g (*i.e.* the per-capita abundance change over time) results from the difference between recruitment rate r and loss rate l, representing the per-capita probability of a new individual entering a population or disappearing, respectively (Fig. 1A). Importantly, the change in growth rate (Δg) is the acceleration or deceleration of abundance change (ΔN) and can be decomposed into the difference between the change in recruitment rate (Δr) and loss rate (Δl, Fig. 1A). The interplay between r and l, and how they change with time (Δr and Δl), remains unknown in real-world populations for most species, particularly at large spatiotemporal scales. Bridging this knowledge gap would provide deeper insights into the mechanisms of the ongoing biodiversity crisis and help shape effective conservation strategies.

Here, we provide a comprehensive assessment of temporal changes in local population abundances of 234 bird species across North America from 1987 to 2021, focusing on acceleration, deceleration, recruitment, and loss. Using 1,033 routes of the North American Breeding Bird Survey (BBS, (*15*)), a long-term, annual, and standardized monitoring program, and advances in N-mixture population models (*14*, *15*), together with full Bayesian inference, we demonstrate widespread bird population declines across North America, pinpoint regions and taxa where population declines accelerate or decelerate, unveil their underlying demographic components, and we show coincidence of the acceleration hotspots with environmental and anthropogenic variables.

Nation-wide decline in abundance. The average change of total bird abundance per route (ΔN, eq. 12) is a significant decline of $\Delta N = -8.62$ individuals per year (95% Credible Interval $(CI) = [-9.88; -7.38]$, histogram in Fig. 2A, Fig. S1A), representing an average loss of 293 birds (out of an average abundance of 2,159 in 1987, *i.e.* 14%) per route from 1987 to 2021. This is in line with the reported decline of bird abundance across North America (*16*) and aligns with trends in some European bird species (*17–22*). Of the 1,033 routes analyzed here, only 26% (265) experienced a significant increase in total bird abundance, and 72% (741) a significant decrease (Fig. S1A). Using a spatial smoother to show average regional trends not obscured by local variation (Fig. 2A), we show that there were only 13 routes located in regions where the smoother shows increasing abundance (dotted black circles Fig. 2A-B) and that bird abundances in Florida, Delaware, New Jersey, and Texas underwent the most pronounced average declines per route.

Regional hotspots of accelerating abundance decline. There was no significant negative or positive Δg at the scale of the US (histogram Fig. 2B, $\Delta g = -3.16 \times 10^{-6}$, $CI = [-4.94 \times 10^{-5}; 4.35 \times 10^{-5}]$). Of the 756 routes with declining abundance there were approximately as many routes with negative as positive Δg (raw, not smoothed estimates), indicative of no trend toward either acceleration or deceleration of the decline (Fig. 2B, Fig. S2B, Fig. S3). The fact that the great majority of the spatially smoothed ΔN is negative (Fig. 2A-B, outside of the black dotted circles) means that the smoothed map of Δg can be interpreted as average regional acceleration ($\Delta g < 0$) and deceleration ($\Delta g > 0$) of the abundance decline (Fig. 2B, outside of the black dotted circles, Fig. S2D). Parts of the Mid-Atlantic region of the US (Delaware, Maryland, and New Jersey), the Midwest (especially Indiana, Ohio, Kentucky, Illinois, Wisconsin, and Michigan), and California had negative smoothed Δg, indicative of an acceleration of the decline in abundance. In these regions, the gap between the number of lost and recruited individuals widens each year, raising concerns about the future of these bird populations. Conversely, the Yukon, most of New England (Connecticut, Massachusetts, Maine, New Hampshire, Rhode Island), Atlantic Canada (New Brunswick, Prince Edward Island, and Nova Scotia), New Mexico, South Carolina, and parts of Georgia and Northern Florida showed a positive Δg, indicating a deceleration of population decline.

Studies have linked declines of bird abundance to agricultural intensification (*17*, *19*, *22–24*) and changes in land-use (*17*, *18*). Our findings support this, as we found that the hotspots of accelerating decline (Fig. 2B) coincide with agricultural areas (namely areas with high fertilizer use and large areas of croplands, Fig. S4, Fig. S5, Fig. S6). This coincidence was stronger for the acceleration (Δg) than for the decline (ΔN) (Fig. 2A-B, Fig. S6). Nonetheless, we suggest that focusing only on the magnitude of the decline may be insufficient to show the impact of agriculture on bird populations, as agriculture can also accelerate the decline (Fig. 2B, Fig. S6). This is concerning, especially, given increases in North American agricultural production, farm size, and mild increases in cropland area during the past 40 years (*25*). Here, we caution that this is a correlative post-hoc analysis, and more robust causal analyses, and perhaps field experiments, are needed to confirm these relationships and better understand their implications.

Changes in recruitment and loss rates. We further demonstrate how changes in loss and recruitment rates contribute to the acceleration of bird abundance decline. At the continental scale, the temporal change of recruitment rate per route was not different from zero (histogram Fig. 2C, $\Delta r = 1.50 \times 10^{-6}$, $\mathrm{CI} = [-2.25 \times 10^{-5}; 2.63 \times 10^{-5}]$, Fig. S1E), suggesting that local net per capita recruitment has not changed at the North American extent since 1987. About 25% of the 1,033 routes showed a significant positive Δr and 25% showed a significant negative Δr. Conversely, change in loss rate was significantly different from zero but the effect was extremely small (histogram Fig. 2D, $\Delta l = 2.53 \times 10^{-5}$, $\mathrm{CI} = [1.72 \times 10^{-7}; 5.06 \times 10^{-5}]$, Fig. S1G), corresponding to an additional loss of 86 individuals per 100,000 birds over the entire time period. The smoothed spatial patterns of Δr (Fig. 2C) and Δl (Fig. 2D) match the spatial patterns of Δg (Fig. 2B), with the Mid-Atlantic region (especially Delaware, Maryland, and New Jersey), the Midwest, and California having a combination of negative Δr and positive Δl. In other words, regions that underwent an increase in loss rate also saw a decrease in recruitment rate, although the correlation is not perfect (Fig. 3A, Fig. S7).

For the 528 routes with a negative Δg, 25% showed a significant positive Δl as the main component of Δg (Fig. S7A, red), while a significant negative Δr was the main component for 15% of these routes (Fig. S7A, orange). Applying the spatial smoother (Fig. 3A) revealed the demographic rates behind the smoothed negative Δg (*i.e.* behind the accelerating decline in the Midwest, Mid-Atlantic, and California, Fig. 2B): Δl was the main component of the decrease in g across the Midwest and California (Fig. 3B, red), whereas Δr dominated across the Mid-Atlantic (Fig. 3B, orange).

Per-species, per-family, and per-habitat analyses. We assessed Δg, Δr and Δl at different levels of taxonomic aggregation: species, family, and preferred habitat. Across 234 species, 66 showed positive ΔN (64 significantly different from zero) of which 77% (51 species) had negative Δg (Fig. 4A-D, red and orange), with significantly dominating negative Δr (67%, 44 species, Fig. 4A-D, orange). Additionally, 21 out of 51 families had positive ΔN (14 significant), of which 95% (20 families) had negative Δg due to significantly negative Δr (Fig. 4D, orange). This indicates that the majority of species and families with increasing abundance are at the same time experiencing a decrease in growth rate, mainly attributed to a decline in recruitment rate. This might be partially a natural process due to density dependent regulation of healthy populations reaching their carrying capacity (*36*, Fig. S8). However, we found that some increasing species experience decline in recruitment that cannot be explained by a negative relationship between N and g (e.g. American Robin, Blue-winged Teal, Fig. 4, Fig. S8); these may still face declines in the future, even though their populations have been increasing.

Importantly, decrease in bird abundance is often directly attributed to the loss of individuals, and conservation policies often aim at reducing this loss. We show, however, that decreases in recruitment rate may be primarily responsible for significant population dynamics, stressing the need to prioritize increasing bird recruitment alongside preventing the loss. The key challenge now is to quantify the relative influence of conservation measures on recruitment and loss to optimize conservation actions and prevent the ongoing recruitment decline. For instance, a decrease in the use of neonicotinoids (*19*, *27*), installation of nest boxes (*28*), or habitat restoration/preservation are policies that may influence both recruitment and loss rates, though we expect them to particularly benefit the former.

Of the 168 species with negative ΔN (163 significant, with the strongest decline often observed for common species such as the House Sparrow, the Chimney Swift, or the Eastern Meadowlark), 52% (88 species) had a significant negative Δg (as many due to Δr as Δl, Fig. 4D), while only 4% (8 species) showed a significant positive Δg. This indicates that more than half of the species with declining abundance are undergoing an acceleration of this decline. Out of the 10 habitats considered here, only 2 had a positive ΔN significantly different from zero (lakes/ponds and forests, Fig. 4C). Conversely, there were 6 habitats with significant declines, with the strongest trends for towns, grasslands, and marshes (Fig. S9). These habitats are significantly impacted by human activities (*29–31*), suggesting a link between the acceleration of the decline and pressures such as urbanization, agricultural intensification, and habitat degradation.

Conclusion. Using one of the most comprehensive and standardized bird time series data in the world, coupled with a model disentangling demographic processes of recruitment and loss, we examined the abundance dynamics and underlying processes for 234 species over 35 years across a continental scale. We reveal geographic hotspots of acceleration of bird abundance decline and attribute these declines to shifts of recruitment and loss since 1987. These hotspots coincide with areas of intense agriculture. We also highlight a worrisome trend: most of the species with increasing populations are experiencing a decrease in recruitment rate. These results are concerning, especially considering growth in human activities across various sectors such as economy, agriculture, or transportation (*5*, *6*, *32–35*).

References

1. IPBES, "Global assessment report on biodiversity and ecosystem services of the Intergovernmental Science-Policy Platform on Biodiversity and Ecosystem Services" (Zenodo, 2019); https://doi.org/10.5281/ZENODO.3831673.
2. C. T. Callaghan, L. Santini, R. Spake, D. E. Bowler, Population abundance estimates in conservation and biodiversity research. *Trends in Ecology & Evolution* **39**, 515–523 (2024).
3. J. Loh, R. E. Green, T. Ricketts, J. Lamoreux, M. Jenkins, V. Kapos, J. Randers, The Living Planet Index: using species population time series to track trends in biodiversity. *Philosophical Transactions of the Royal Society B: Biological Sciences* **360**, 289–295 (2005).
4. D. H. Meadows, J. Randers, D. L. Meadows, "The Limits to Growth (1972)" in *The Future of Nature*, L. Robin, S. Sörlin, P. Warde, Eds. (Yale University Press, 2017; https://www.degruyter.com/document/doi/10.12987/9780300188479-012/html), pp. 101–116.
5. T. Piketty, *Capital in the Twenty-First Century* (Harvard University Press, 2014; https://www.degruyter.com/document/doi/10.4159/9780674369542/html).
6. W. Steffen, W. Broadgate, L. Deutsch, O. Gaffney, C. Ludwig, The trajectory of the Anthropocene: The Great Acceleration. *The Anthropocene Review* **2**, 81–98 (2015).
7. A. D. Barnosky, N. Matzke, S. Tomiya, G. O. U. Wogan, B. Swartz, T. B. Quental, C. Marshall, J. L. McGuire, E. L. Lindsey, K. C. Maguire, B. Mersey, E. A. Ferrer, Has the Earth's sixth mass extinction already arrived? *Nature* **471**, 51–57 (2011).
8. G. Ceballos, P. R. Ehrlich, A. D. Barnosky, A. García, R. M. Pringle, T. M. Palmer, Accelerated modern human–induced species losses: Entering the sixth mass extinction. *Sci. Adv.* **1**, e1400253 (2015).
9. M. C. Urban, Accelerating extinction risk from climate change. *Science* **348**, 571–573 (2015).
10. A. C. Studeny, S. T. Buckland, P. J. Harrison, J. B. Illian, A. E. Magurran, S. E. Newson, Fine-tuning the assessment of large-scale temporal trends in biodiversity using the example of British breeding birds. *Journal of Applied Ecology* **50**, 190–198 (2013).
11. S. t Buckland, A. e Magurran, R. e Green, R. m Fewster, Monitoring change in biodiversity through composite indices. *Philosophical Transactions of the Royal Society B: Biological Sciences* **360**, 243–254 (2005).
12. R. M. Fewster, S. T. Buckland, G. M. Siriwardena, S. R. Baillie, J. D. Wilson, Analysis of population trends for farmland birds using Generalized Additive Models. *Ecology* **81**, 1970–1984 (2000).
13. D. Dail, L. Madsen, Models for Estimating Abundance from Repeated Counts of an Open Metapopulation. *Biometrics* **67**, 577–587 (2011).
14. M. Kéry, J. A. Royle, *Applied Hierarchical Modeling in Ecology: Analysis of Distribution, Abundance and Species Richness in R and BUGS: Volume 2: Dynamic and Advanced Models* (Academic Press, Cambridge, 1st edition., 2020).
15. D. Ziolkowski Jr., M. Lutmerding, V. Aponte, M.-A. Hudson, 2022 Release - North American Breeding Bird Survey Dataset (1966-2021), U.S. Geological Survey (2022); https://doi.org/10.5066/P97WAZE5.

16. K. V. Rosenberg, A. M. Dokter, P. J. Blancher, J. R. Sauer, A. C. Smith, P. A. Smith, J. C. Stanton, A. Panjabi, L. Helft, M. Parr, P. P. Marra, Decline of the North American avifauna. *Science* **366**, 120–124 (2019).
17. D. E. Bowler, H. Heldbjerg, A. D. Fox, M. De Jong, K. Böhning-Gaese, Long-term declines of European insectivorous bird populations and potential causes. *Conservation Biology* **33**, 1120–1130 (2019).
18. S. Fraixedas, A. Lindén, K. Meller, Å. Lindström, O. Keišs, J. A. Kålås, M. Husby, A. Leivits, M. Leivits, A. Lehikoinen, Substantial decline of Northern European peatland bird populations: Consequences of drainage. *Biological Conservation* **214**, 223–232 (2017).
19. C. A. Hallmann, R. P. B. Foppen, C. A. M. Van Turnhout, H. De Kroon, E. Jongejans, Declines in insectivorous birds are associated with high neonicotinoid concentrations. *Nature* **511**, 341–343 (2014).
20. R. Inger, R. Gregory, J. P. Duffy, I. Stott, P. Voříšek, K. J. Gaston, Common European birds are declining rapidly while less abundant species' numbers are rising. *Ecology Letters* **18**, 28–36 (2015).
21. I. Newton, The recent declines of farmland bird populations in Britain: an appraisal of causal factors and conservation actions. *Ibis* **146**, 579–600 (2004).
22. S. Rigal, V. Dakos, H. Alonso, A. Auniņš, Z. Benkő, L. Brotons, T. Chodkiewicz, P. Chylarecki, E. de Carli, J. C. del Moral, C. Domşa, V. Escandell, B. Fontaine, R. Foppen, R. Gregory, S. Harris, S. Herrando, M. Husby, C. Ieronymidou, F. Jiguet, J. Kennedy, A. Klvaňová, P. Kmecl, L. Kuczyński, P. Kurlavičius, J. A. Kålås, A. Lehikoinen, Å. Lindström, R. Lorrillière, C. Moshøj, R. Nellis, D. Noble, D. P. Eskildsen, J.-Y. Paquet, M. Pélissié, C. Pladevall, D. Portolou, J. Reif, H. Schmid, B. Seaman, Z. D. Szabo, T. Szép, G. T. Florenzano, N. Teufelbauer, S. Trautmann, C. van Turnhout, Z. Vermouzek, T. Vikstrøm, P. Voříšek, A. Weiserbs, V. Devictor, Farmland practices are driving bird population decline across Europe. *Proceedings of the National Academy of Sciences* **120**, e2216573120 (2023).
23. R. E. Green, S. J. Cornell, J. P. W. Scharlemann, A. Balmford, Farming and the Fate of Wild Nature. *Science* **307**, 550–555 (2005).
24. R. L. Stanton, C. A. Morrissey, R. G. Clark, Analysis of trends and agricultural drivers of farmland bird declines in North America: A review. *Agriculture, Ecosystems & Environment* **254**, 244–254 (2018).
25. P. Potapov, S. Turubanova, M. C. Hansen, A. Tyukavina, V. Zalles, A. Khan, X.-P. Song, A. Pickens, Q. Shen, J. Cortez, Global maps of cropland extent and change show accelerated cropland expansion in the twenty-first century. *Nat Food* **3**, 19–28 (2021).
26. R. M. May, Togetherness among Schistosomes: its effects on the dynamics of the infection. *Mathematical Biosciences* **35**, 301–343 (1977).
27. Y. Li, R. Miao, M. Khanna, Neonicotinoids and decline in bird biodiversity in the United States. *Nat Sustain* **3**, 1027–1035 (2020).
28. A. P. Møller, F. Adriaensen, A. Artemyev, J. Bańbura, E. Barba, C. Biard, J. Blondel, Z. Bouslama, J. Bouvier, J. Camprodon, F. Cecere, A. Chaine, A. Charmantier, M. Charter, M. Cichoń, C. Cusimano, D. Czeszczewik, B. Doligez, C. Doutrelant, A. Dubiec, M. Eens, T. Eeva, B. Faivre, P. N. Ferns, J. T. Forsman, E. García-del-Rey, A. Goldshtein, A. E. Goodenough, A. G. Gosler, I. Góźdź, A. Grégoire, L. Gustafsson, I. R. Hartley, P. Heeb, S. A. Hinsley, P. Isenmann, S. Jacob, A. Järvinen, R. Juškaitis, W. Kania, E. Korpimäki, I. Krams, T. Laaksonen, B. Leclercq, E. Lehikoinen, O. Loukola, A. Lundberg, M. C. Mainwaring, R. Mänd, B. Massa, T. D. Mazgajski, S. Merino, C. Mitrus, M. Mönkkönen, J. Morales-Fernaz, J. Moreno, X. Morin, R. G. Nager, J. Nilsson, S. G. Nilsson, A. C. Norte, M. Orell, P. Perret, C. M. Perrins, C. S. Pimentel, R. Pinxten, I. Priedniece, M. Quidoz, V. Remeš, H. Richner, H. Robles, A. Russell, S. Rytkönen, J. C. Senar, J. T. Seppänen, L. Pascoal Da Silva, T. Slagsvold, T. Solonen, A. Sorace, M. J. Stenning, J. Török, P. Tryjanowski, A. J. Van Noordwijk, M. Von Numers, W. Walankiewicz, M. M. Lambrechts, Clutch-size variation in Western Palaearctic secondary hole-nesting passerine birds in relation to nest box design. *Methods Ecol Evol* **5**, 353–362 (2014).

29. L. A. Brennan, W. P. Kuvlesky, North american grassland birds: an unfolding conservation crisis? *Journal of Wildlife Management* **69**, 1–13 (2005).
30. J. M. Marzluff, "Worldwide urbanization and its effects on birds" in *Avian Ecology and Conservation in an Urbanizing World*, J. M. Marzluff, R. Bowman, R. Donnelly, Eds. (Springer US, Boston, MA, 2001; http://link.springer.com/10.1007/978-1-4615-1531-9_2), pp. 19–47.
31. N. C. Davidson, How much wetland has the world lost? Long-term and recent trends in global wetland area. *Mar. Freshwater Res.* **65**, 934 (2014).
32. K. C. Seto, B. Güneralp, L. R. Hutyra, Global forecasts of urban expansion to 2030 and direct impacts on biodiversity and carbon pools. *Proc. Natl. Acad. Sci. U.S.A.* **109**, 16083–16088 (2012).
33. D. Tilman, J. Fargione, B. Wolff, C. D'Antonio, A. Dobson, R. Howarth, D. Schindler, W. H. Schlesinger, D. Simberloff, D. Swackhamer, Forecasting Agriculturally Driven Global Environmental Change. *Science* **292**, 281–284 (2001).
34. J. A. Foley, N. Ramankutty, K. A. Brauman, E. S. Cassidy, J. S. Gerber, M. Johnston, N. D. Mueller, C. O'Connell, D. K. Ray, P. C. West, C. Balzer, E. M. Bennett, S. R. Carpenter, J. Hill, C. Monfreda, S. Polasky, J. Rockström, J. Sheehan, S. Siebert, D. Tilman, D. P. M. Zaks, Solutions for a cultivated planet. *Nature* **478**, 337–342 (2011).
35. E. C. Ellis, K. Klein Goldewijk, S. Siebert, D. Lightman, N. Ramankutty, Anthropogenic transformation of the biomes, 1700 to 2000. *Global Ecology and Biogeography* **19**, 589–606 (2010).

Acknowledgements

This study stands on the shoulders of the thousands of volunteers who participated in the North American BBS, and the institutions that manage this program. The authors thank the Ohio Supercomputer Center for their computational resources. We thank three anonymous reviewers for their helpful comments. **Funding:** F.L. and P.K. were funded by the European Union (ERC, BEAST, 101044740). Views and opinions expressed are however those of the author(s) only and do not necessarily reflect those of the European Union or the European Research Council Executive Agency. Neither the European Union nor the granting authority can be held responsible for them. M.A.J. was supported by the National Science Foundation DEB-1926598 and OISE-2330423. P.K. received funding from by the Czech Science Foundation (project number: 24-14299L). **Author Contributions:** All authors conceived the idea of the paper; F.L, and P.K. conducted analyses; all authors wrote the paper. **Competing interest:** All authors declare no competing interests. **Data and materials availability:** All data and software are archived and available on Zenodo (*40*).

Supplementary materials

Materials and Methods
Figs. S1 to S8
Table S1
Data and code: https://doi.org/10.5281/zenodo.14593916

Figures

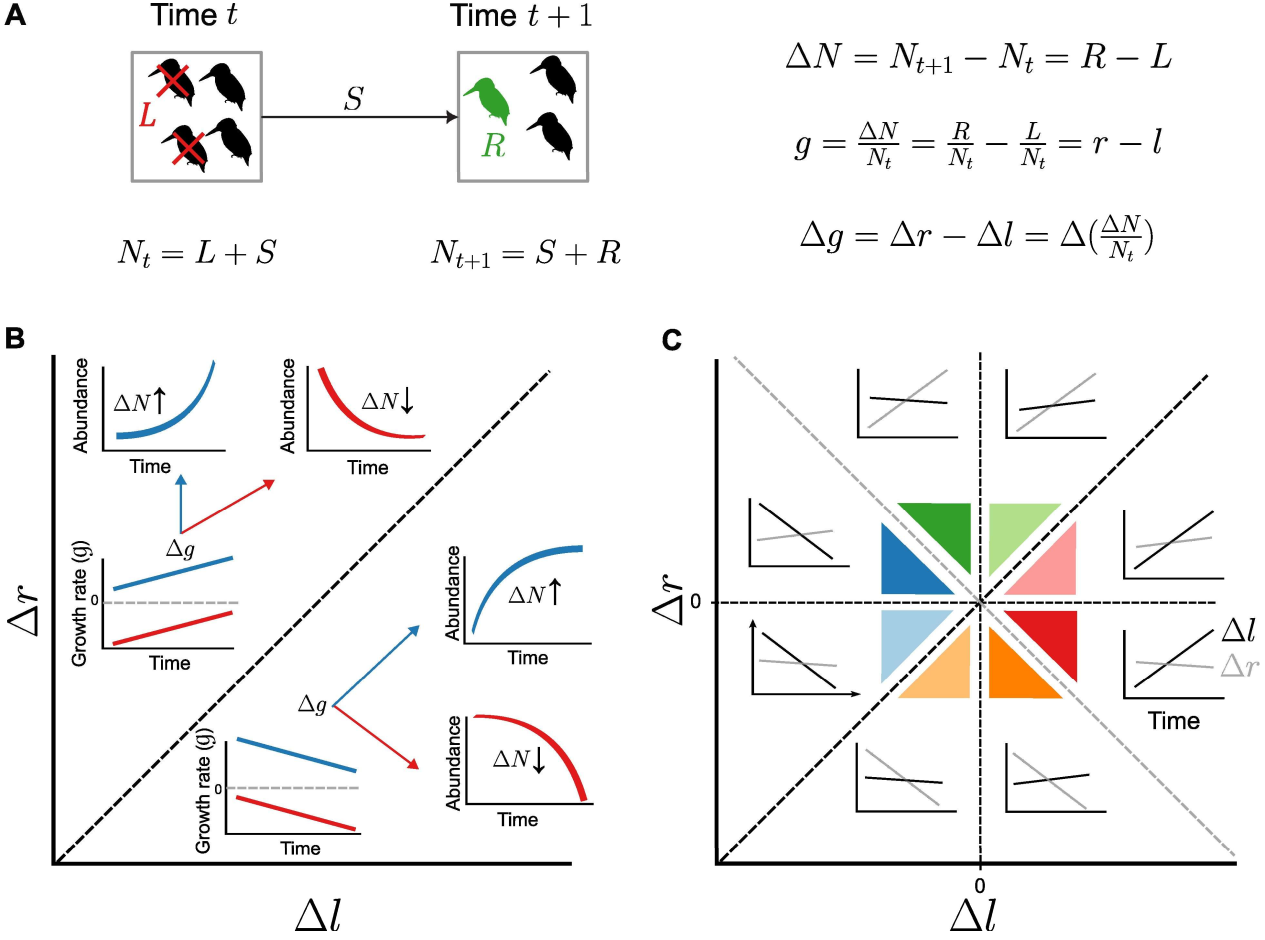

Fig. 1 | Components of temporal change of abundance. (A) Relations between individual abundance (N), number of lost individuals (L, death or emigration), recruited individuals (R, birth or immigration), survivors (S), and change in abundance (ΔN). They can be expressed as per-capita rates: yearly growth rate (g), recruitment rate (r), loss rate (l), and their respective change (Δg, Δr, Δl). Importantly, Δg is indicative of acceleration or deceleration of ΔN. (B) Each sampling location, species, family, or habitat type can be mapped onto a Δl vs Δr space. Above the black dashed diagonal, growth rate increases (i.e. positive Δg); below, growth rate declines (i.e. negative Δg). Arrows (↑ and ↓) indicate abundance increases (positive ΔN) and declines (negative ΔN). (C) In the same Δl vs Δr space, colors indicate the dominant process: blue is dominant negative Δl, green is dominant positive Δr, orange is dominant negative Δr and, red is dominant positive Δl. Inset plots show Δl (black line) and Δr (grey line).

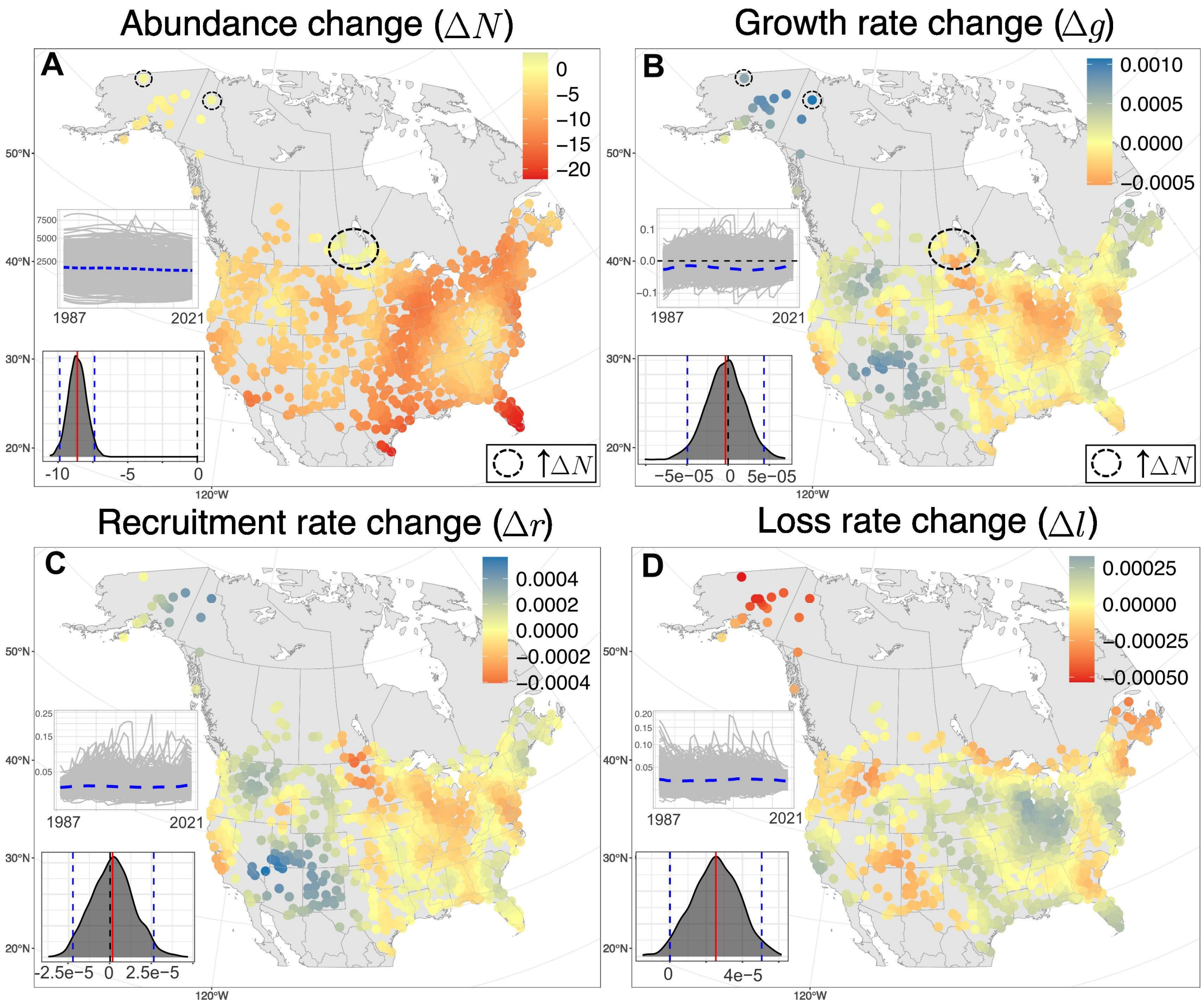
Abundance change (ΔN)

Growth rate change (Δg)

Recruitment rate change (Δr)

Loss rate change (Δl)

Fig. 2 | Temporal change of abundance and vital rates. (A) Temporal change in total bird abundance from 1987 to 2021, and (B) temporal change of yearly growth rate decomposed into (C) temporal change of recruitment rate, and (D) temporal change of loss rate. Maps in all panels are estimates from the *N*-mixture model, smoothed using a spatial GAM; for raw (not spatially smoothed) values see Fig. S1. Since abundances are decreasing across most of North America (A) the red regions in panel (B) are regional hotspots of acceleration of bird abundance decline. Dashed circles mark the few routes with positive values of the smoothened ΔN. Inset plots in bottom left show the raw (i.e. not spatially smoothed) trends in abundance, growth, recruitment, and loss rates; y-axes have been square root transformed, with the average trend in blue dashed line. The histograms show the posterior distributions of the grand slope; red vertical lines are means and dashed blue lines are 95% credible intervals.

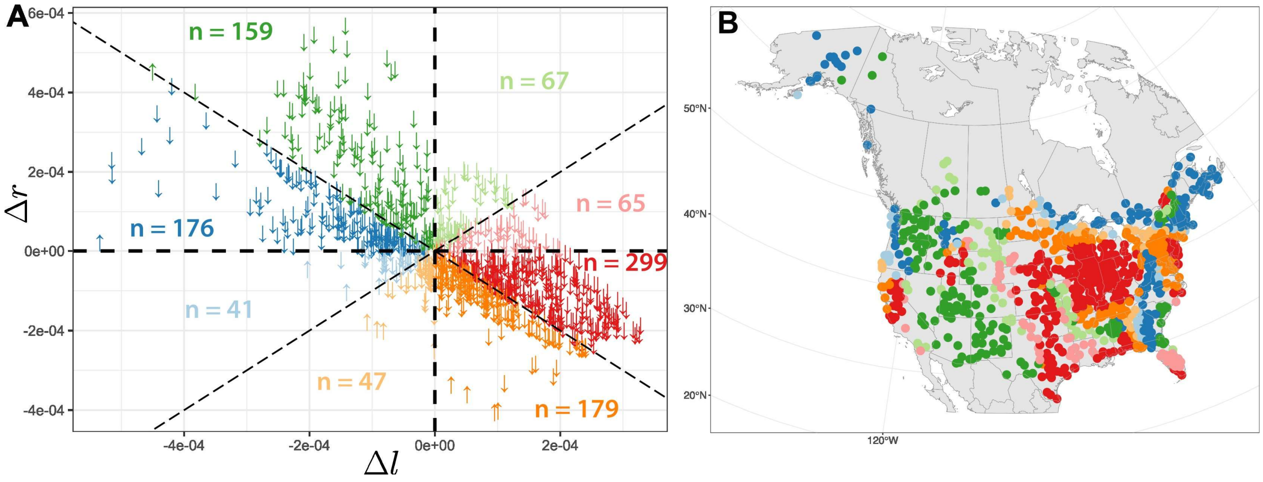

Fig. 3 | Eight classes of temporal change of vital rates across North America. Colors correspond to classes in Fig. 1C. (A) Loss rate change (Δl) versus recruitment rate change (Δr) from the smoothened maps in Fig. 2C-D. Each arrow is a route, ↑ is an increase of total abundance change (positive ΔN), ↓ is a decrease (negative ΔN). Plots with raw (not smoothened) values are in supplementary material (Fig. S7). (B) Spatial representation of those values.

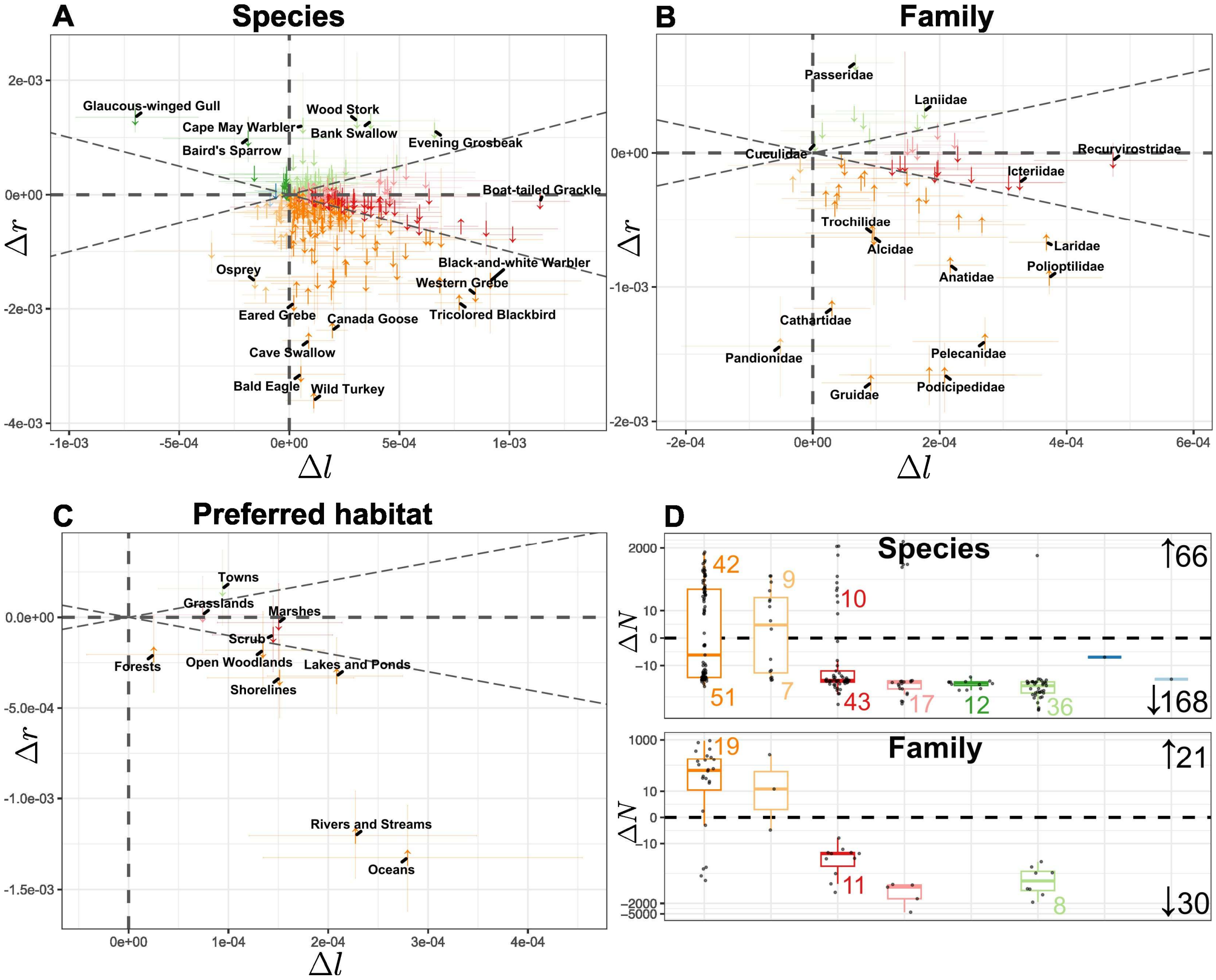

Fig. 4 | Temporal change of vital rates aggregated to species, family, and habitat levels. (A) Loss rate change (Δl) vs recruitment rate change (Δr) where each arrow is one of the 234 analyzed bird species; (B) each arrow is one of the 51 avian families; (C) each arrow is one of the 10 habitats. Arrows indicate abundance change (↑ positive and ↓ negative ΔN). Error bars around each arrow are 95% credible intervals of Δl and Δr. (D) Numbers of increasing (above 0) and decreasing (below 0) abundance (ΔN) on a $\log_{10}$ scale, colored by each Δl vs. Δr class for bird species (top panel) and families (bottom panel). Colors indicate the dominant process: blue is dominant negative Δl, green is dominant positive Δr, orange is dominant negative Δr and, red is dominant positive Δl (see Fig. 1 for details).

Supplementary Materials for

Hotspots of acceleration and demographic processes behind decline of North American birds

François Leroy*, Marta A. Jarzyna, Petr Keil

*Correspondence to: leroy@fzp.czu.cz

This PDF file includes:

Materials and Methods
Figs. S1 to S9
Table S1
References 36-57

Other Supplementary Materials for this manuscript include the following:

Data and code: https://doi.org/10.5281/zenodo.14593916

Materials and Methods

Data. To investigate patterns of population dynamics of birds in North America, we used the North American Breeding Bird Survey (*16*, hereafter BBS), an ongoing bird monitoring initiative launched in 1966. Spanning more than 50 years, the BBS comprises 39.2 km-long routes scattered across the contiguous United States and Canada, each divided into 50 census points at approximately 800 m intervals. From its inception with about 500 routes in 1966, the BBS has grown to encompass 5,581 routes by 2021. At the time of our data download on September 5, 2022, the data contained 6,946,871 records of species abundances compiled by 10,316 volunteers for 746 species and spanning over 50 years. The BBS data also contain meteorological data, date, hour, and spatial coordinates.

Routes with long time-series (e.g. from 1969 to 2021) were spatially sparse. To balance long temporal extent with robust spatial coverage, we focused our analysis on the 1987-2021 period and selected routes with no more than 15 years of missing data.

For each species, we extracted the preferred habitat from the eBird/Cornell online database (*36*). These were: Towns, Grasslands, Shorelines, Scrubs, Deserts, Rivers and Streams, Marshes, Open Woodlands, Forests, Lakes and Ponds, Oceans, and Tundra. Species with missing habitat data (23 in total) were excluded. In the end, we performed our analysis using 1,033 routes from 1987 to 2021 (*i.e.* 35 years), with 1,623,394 occurrences of 564 species.

Dynamic *N*-mixture model. We modelled the abundance of each of the 564 bird species across each route and year from 1987 to 2021 using a dynamic *N*-mixture model (*13*), hereafter the DM model (Dail & Madsen). It is a generalization of the *N*-mixture model by Royle (*37*) that assumes open populations (*i.e.* metapopulations can experience births, immigrations, deaths, or emigrations) and that has been successfully applied to data similar to the BBS (*13*, *14*). While the DM model can accommodate repeated counts, we did not use them primarily for computational feasibility (*14*).

For a species j and a route i, the abundance at time $t+1$ (*i.e.* $N_{j,i,t+1}$) is the sum of surviving individuals ($S_{j,i,t+1}$) from the previous year and newly recruited individuals ($R_{j,i,t+1}$):

$$N_{j,i,t+1} = S_{j,i,t+1} + R_{j,i,t+1} \qquad \text{eq. 1}$$

Survival and recruitment are modeled separately. The number of surviving individuals $S_{j,i,t+1}$, is assumed to follow a Binomial distribution:

$$S_{j,i,t+1} \sim Binomial(N_{j,i,t}, \phi_{j,i,t}) \qquad \text{eq. 2}$$

Where $N_{j,i,t}$ is the abundance of species j at route i and time t, and $\phi_{j,i,t}$ is the probability that an individual survives from t to $t+1$.

Similarly, recruitment $R_{j,i,t+1}$, follows a Poisson distribution:

$$R_{j,i,t+1} \sim Poisson(\gamma_{j,i,t}) \qquad \text{eq. 3}$$

where $\gamma_{j,i,t}$ is the expected number of recruited individuals. The abundance at time 1 ($N_{j,i,1}$) is:

$$N_{j,i,1} \sim Poisson(\lambda_{j,i,1}), \qquad \text{eq. 4}$$

where $\lambda_{j,i,1}$ is the mean abundance of the species j at route i at time 1.

To correct for imperfect detection, the *observed* count ($C_{j,i,t}$) is modelled as a Binomial random variable, conditional on the true abundance ($N_{j,i,t}$):

$$C_{j,i,t} \sim B\text{inomial}(N_{j,i,t}, p_{j,i,t}) \text{ eq. 5}$$

Here, $p_{\mathrm{j,i,t}}$ is the species-specific probability of detecting an individual. The detection probability is modelled on the logit scale:

$$logit(p_{j,i,t}) = \alpha + \boldsymbol{x}_{j,i,t}^{\mathrm{T}}\boldsymbol{b}, \quad \text{eq. 6}$$

where α is the intercept, $\boldsymbol{x}^{\mathrm{T}}$ is the transpose of a vector of covariates, and $\boldsymbol{b}$ is a vector of regression coefficients. The covariates $\boldsymbol{x}$ include: the exact time of the day of the census (in decimal hours), and weather data, *i.e.* wind condition (ordinal variable with 9 levels ranging from < 2 km.h^{-1} to 74 km.h^{-1}), sky condition (factor with 7 levels: clear sky, partly cloudy, cloudy, fog, drizzle, snow, and shower), and average temperature during the census (in °C). Missing values for the time of the day and temperature were imputed following Kéry and Royle (2015), by sampling from a normal distribution:

$$x_{i,t} \sim N(\mu, \sigma) \text{ eq. 7}$$

where μ and σ are means and standard deviation of observed data for the respective covariate. An implementation of the model in JAGS programming language (*39*) is in the Zenodo repository (*40*).

For each *j*-th species, we fitted the DM model in a Bayesian framework using MCMC sampler JAGS (Plummer, 2003; https://mcmc-jags.sourceforge.io/), interfaced through the package jagsUI (*41*) in R ver. 4.2.1 (*42*). For all the parameters, we used normal distributions with 0 mean and variance of 100 (Appendix B). The settings for the MCMC algorithm were: 3 chains, 100,000 iterations per chain, 75,000 burn-in, a thinning rate of 10, and 1,000 iterations in the adaptative phase. The entire fitting procedure for all 564 species (1 core per MCMC chain, 3 chains per species) required approximately 2 days on 1,692 cores of the Ohio Supercomputer Center (https://www.osc.edu/), each core operating at 2.5 GHz.

We assessed the convergence of the DM models for each species by computing the $\hat{R}$ (Rhat, Gelman & Rubin, 1992) for all of the 106,419 monitored values. Following standard practice (Gelman & Rubin, 1992), we only retained the most reliable models with median $\hat{R} \leq 1.1$ of all the 106,419 monitored values, which led to a final set of 234 species for further analysis. Among these, the average median $\hat{R}$ was 1.03, with a standard deviation of 0.03. The reduction from the initial 564 species reflects the complexity of the DM model, which can lead to the unidentifiability of certain parameters in some models, especially for rare species with limited presence and low abundance.

To some, it may seem counterintuitive that recruitment and loss is estimated merely from abundance counts. We refer those readers to (*13*) and (*14*) for details on how this works. In addition, we provide a didactical simplified version of the model in the Zenodo repository of this article (*40*); in it, we first show how artificial abundance time series can be simulated from the model, given a set of parameters representing recruitment and loss. Second, we demonstrate how these parameters can be correctly estimated, given the model and the abundance time series data.

Demographic rates. From the output of the DM model and for each j-th species at i-th site and t-th year (starting from 1988), we derived the yearly number of lost individuals L, as well as the per-capita growth rate g, per-capita recruitment rate r, and per-capita loss rate l:

$$L_{j,i,t+1} = N_{j,i,t} - S_{j,i,t+1} \qquad \text{eq. 8}$$

$$g_{j,i,t+1} = \frac{N_{j,i,t+1} - N_{j,i,t}}{N_{j,i,t}} = \frac{\Delta N}{N_t} \qquad \text{eq. 9}$$

$$r_{j,i,t+1} = \frac{R_{j,i,t+1}}{N_{j,i,t}} \qquad \text{eq. 10}$$

$$l_{j,i,t+1} = \frac{L_{j,i,t+1}}{N_{j,i,t}} \qquad \text{eq. 11}$$

Per route, per species, per family and per habitat analyses. We assessed all metrics at different levels of taxonomic aggregation. First, for each route, we aggregated the number of individuals, recruitments, or losses of all the species together and assessed these aggregated rates. Conversely, for each species, family or preferred habitat, we aggregated those metrics over all the routes. In other words, these were not mapped geographically as in the spatial analysis, but the numbers were aggregated for each grouping (species, family, habitat) over all 1,033 routes included in our analysis.

In the DM model, each value of $N_{j,i,t}$, $S_{j,i,t}$, $R_{j,i,t}$ (and thus $L_{j,i,t}$) for each species j, site i, and time t is estimated with a posterior distribution. To propagate the uncertainty of these estimates to the higher levels of aggregations (namely route, family and preferred habitat), we sampled each of those posterior distributions 500 times. For each sample, we aggregated those values per route, species, family or preferred habitat. This gave us a new posterior distribution of N, R and L with a mean ($y_{j,t}$) and standard deviation ($sd_{j,t}$) at the desired level of aggregation. We performed the same propagation of uncertainty for the rates g, r, and l across all the levels of aggregation.

Temporal change with Bayesian mixed models. We assessed the temporal change of the estimated N, g, r, and l for the different levels of aggregation while propagating the uncertainty of these estimates from the posteriors of the DM model, using mixed models. We used a random varying slope and intercept for each route, species, family or preferred habitat:

$$y_{j,t} = \Delta y_j \times t + \beta_{0_j} + \epsilon_{j,t}, \qquad \text{eq. 12}$$

where $y_{j,t}$ is the mean of the posterior distribution (see previous paragraph) estimated by the DM model, Δy_j and β_{0_j} are the random slopes and intercepts, j is the index of the level of aggregation (e.g. j-th route) and t the year in the time series. The error term $\epsilon_{j,t}$ comes from a normal distribution

$$\epsilon_{j,t} \sim N\left(0, sd_{j,t}\right), \qquad \text{eq. 13}$$

where $sd_{j,t}$ is the standard deviation of the posterior distribution of $y_{j,t}$ estimated in the DM model (see previous paragraph). This way, the per-species uncertainty of all the y metrics (estimated in the DM model) is propagated to the mixed effect model of temporal trends, an approach used in meta analyses (*44*). Finally, the random slopes Δy_j and intercepts β_{0_j} come from normal distributions:

$$\Delta y_j \sim N(M_{\Delta y}, SD_{\Delta y}) \text{ eq. 14}$$

$$\beta_{0_j} \sim N(M_{\beta_0}, SD_{\beta_0}) \text{ eq. 15}$$

The posterior distributions of $M_{\Delta y}$ and M_{β_0}represent the grand means of the trends and describe the overall temporal trend across all js.

Spatial smoothing. For the spatial analysis, mapping the above-mentioned temporal changes (ΔN, $\Delta g, \Delta l$, Δr) may reveal a substantial local variation among individual routes, which could obscure average trends across larger regions. To detect these regional anomalies, we smoothed the variation of the rates using spatial generalized additive models (GAM) using the R package mgcv (*45*):

$$\Delta y_j = \mathrm{s}(Lon_j, Lat_j), \text{ eq. 16}$$

with Δy_j the temporal change of the metric considered at route j, Lon and Lat the longitude and latitude of the route j, and $s()$ indicating that longitude and latitude are treated as interacting covariates in the spline function of the smoother. For the spline function, we used a gaussian process as a smooth class (argument “bs” of the $s()$ function in mgcv) with 100 basis functions (approximately $\frac{1}{10}^{th}$ of the number of routes).

Classification of acceleration and deceleration. The same Δg value can emerge from different combinations of Δl and Δr; that is, acceleration or deceleration of ΔN can result from increases or decreases in per-capita loss, recruitment, or both. To capture this complexity, we devised a classification system for temporal population dynamics based on Δl and Δr (Fig. 1B, 1C), which allowed us to show the relative importance of Δl and Δr in a single map. We created a color scheme where each route (or species, family, or preferred habitat) lays in a 2-dimensional space with Δl on the x-axis and Δr on the y-axis (henceforth Δl - Δr space). For instance, our analysis reveals that at the route level, the average ΔN is negative (indicated by ↓). In this case, blue and green hues indicate deceleration of population decline (Fig. 1C), which can be mainly attributed to either a negative Δl (blue) or to a positive Δr (green). Conversely, still in the case of a negative ΔN (↓), red and orange hues indicate an acceleration of the decline, and that either a positive Δl (red) or a negative Δr (orange) is the main component of the acceleration. This classification was applied to individual routes, as well as to smoothed averages. We note that for positive ΔN (indicate by ↑), implications of the color scheme are slightly different (*i.e.* either acceleration or deceleration of increasing population), but the interpretation about positive or negative Δr and Δl remains consistent.

Interpreting patterns of change. To interpret the patterns of acceleration, we performed a post-hoc analysis of coincidence between hotspots of ΔN, Δg, Δr, and Δl (Fig. 2) with several environmental and human-related variables. We obtained raster data on land cover, cropland area and its temporal change, fertilizer usage, vegetation greenness and its change, net primary productivity, climate, temperature change, human footprint and its temporal change, human population density, and elevation (Table S1). We aggregated some of these rasters to a coarser resolution (mostly those which originally came at a 30 sec resolution) to better represent regional means, since the smoothened demographic rates also represent regional means. The original and coarsened resolutions are listed in Table S1. The aggregation function was either sum (for areas of land cover classes and cropland area) or arithmetic mean (for the rest of variables). We then overlaid the BBS routes over each coarsened raster, and calculated the mean value of all pixels overlapping each route. We plotted all bivariate relationships between the covariates and ΔN, Δg, Δr, and Δl (both raw and smoothened) across the 1,033 BBS routes, together with their Spearman correlations (Figure S4).

We conducted four random forest (*46*) analyses using the randomForest R package (*47*) with the default settings of hyperparameters (as of ver. 4.7.1.2), where the response variable was the smoothed ΔN, Δg, Δr, or Δl per route. As predictors we used the variables from Table S1. If there were two or more predictors with Spearman correlation exceeding 0.5 (Fig. S4), we only chose one of them for the random forest analyses, ending up with 11 predictors (Fig. S6). If a variable was found to be important in the random forest, we interpreted its effect as also potentially attributable to the other discarded variables. We evaluated variable importance by computing the mean decrease in accuracy while permuting the out-of-bag (OOB) data for each tree in the forest. The resulting variable importance rankings are in Fig. S6.

Supplementary References

36. Cornell Lab of Ornithology, All About Birds (2019). https://www.allaboutbirds.org.
37. J. A. Royle, N-Mixture Models for Estimating Population Size from Spatially Replicated Counts. *Biometrics* **60**, 108–115 (2004).
38. M. Kéry, J. A. Royle, *Applied Hierarchical Modeling in Ecology: Analysis of Distribution, Abundance and Species Richness in R and BUGS: Volume 1:Prelude and Static Models* (Academic Press, Amsterdam ; Boston, 1st edition., 2015).
39. M. Plummer, JAGS: A program for analysis of Bayesian graphical models using Gibbs sampling. In K. Hornik, F. Leisch, & A. Zeileis (Eds.), Proceedings of the 3rd International Workshop on Distributed Statistical Computing, 124(125.10), 1–10. (2003).
40. F. Leroy, M. Jarzyna, P. Keil, Zenodo Version 1.0.2; https://doi.org/10.5281/zenodo.14593916.
41. K. Kellner, *jagsUI: A Wrapper Around "rjags" to Streamline "JAGS" Analyses* (2021; https://CRAN.R-project.org/package=jagsUI).
42. R Core Team, *R: A Language and Environment for Statistical Computing* (R Foundation for Statistical Computing, Vienna, Austria, 2021; https://www.R-project.org/).
43. A. Gelman, D. B. Rubin, Inference from Iterative Simulation Using Multiple Sequences. *Statist. Sci.* **7** (1992).
44. W. Viechtbauer, Conducting Meta-Analyses in *R* with the **metafor** Package. *J. Stat. Soft.* **36** (2010).
45. S. N. Wood, Fast stable restricted maximum likelihood and marginal likelihood estimation of semiparametric generalized linear models. *Journal of the Royal Statistical Society (B)* **73**, 3–36 (2011).
46. L. Breiman, Random Forests. *Machine Learning* **45**, 5–32 (2001).
47. A. Liaw, M. Wiener, Classification and Regression by randomForest. *R News* **2**, 18–22 (2002).
48. D. Zanaga, R. Van De Kerchove, W. De Keersmaecker, N. Souverijns, C. Brockmann, R. Quast, J. Wevers, A. Grosu, A. Paccini, S. Vergnaud, O. Cartus, M. Santoro, S. Fritz, I. Georgieva, M. Lesiv, S. Carter, M. Herold, L. Li, N.-E. Tsendbazar, F. Ramoino, O. Arino, ESA WorldCover 10 m 2020 v100, version v100, Zenodo (2021); https://doi.org/10.5281/ZENODO.5571936.
49. M. Zhao, S. W. Running, Drought-Induced Reduction in Global Terrestrial Net Primary Production from 2000 Through 2009. *Science* **329**, 940–943 (2010).
50. R. J. Hijmans, S. E. Cameron, J. L. Parra, P. G. Jones, A. Jarvis, Very high resolution interpolated climate surfaces for global land areas. *Int. J. Climatol.* **25**, 1965–1978 (2005).
51. H. I. Reuter, A. Nelson, A. Jarvis, An evaluation of void-filling interpolation methods for SRTM data. *International Journal of Geographical Information Science* **21**, 983–1008 (2007).
52. N. J. L. Lenssen, G. A. Schmidt, J. E. Hansen, M. J. Menne, A. Persin, R. Ruedy, D. Zyss, Improvements in the GISTEMP Uncertainty Model. *JGR Atmospheres* **124**, 6307–6326 (2019).
53. N. Lenssen, G. A. Schmidt, M. Hendrickson, P. Jacobs, M. J. Menne, R. Ruedy, A NASA GISTEMPv4 Observational Uncertainty Ensemble. *JGR Atmospheres* **129**, e2023JD040179 (2024).
54. P. Potter, N. Ramankutty, E. M. Bennett, S. D. Donner, Characterizing the Spatial Patterns of Global Fertilizer Application and Manure Production. *Earth Interactions* **14**, 1–22 (2010).
55. K. C. GUAY, P. S. A. BECK, S. J. GOETZ, Long-Term Arctic Growing Season NDVI Trends from GIMMS 3g, 1982-2012. ORNL Distributed Active Archive Center [Preprint] (2015). https://doi.org/10.3334/ORNLDAAC/1275.
56. O. Venter, E. W. Sanderson, A. Magrach, J. R. Allan, J. Beher, K. R. Jones, H. P. Possingham, W. F. Laurance, P. Wood, B. M. Fekete, M. A. Levy, J. E. M. Watson, Global terrestrial Human Footprint maps for 1993 and 2009. *Sci Data* **3**, 160067 (2016).
57. Center For International Earth Science Information Network-CIESIN-Columbia University, Documentation for the Gridded Population of the World, Version 4 (GPWv4), Revision 11 Data

Sets. Palisades, NY: NASA Socioeconomic Data and Applications Center (SEDAC) [Preprint] (2018). https://doi.org/10.7927/H45Q4T5F.

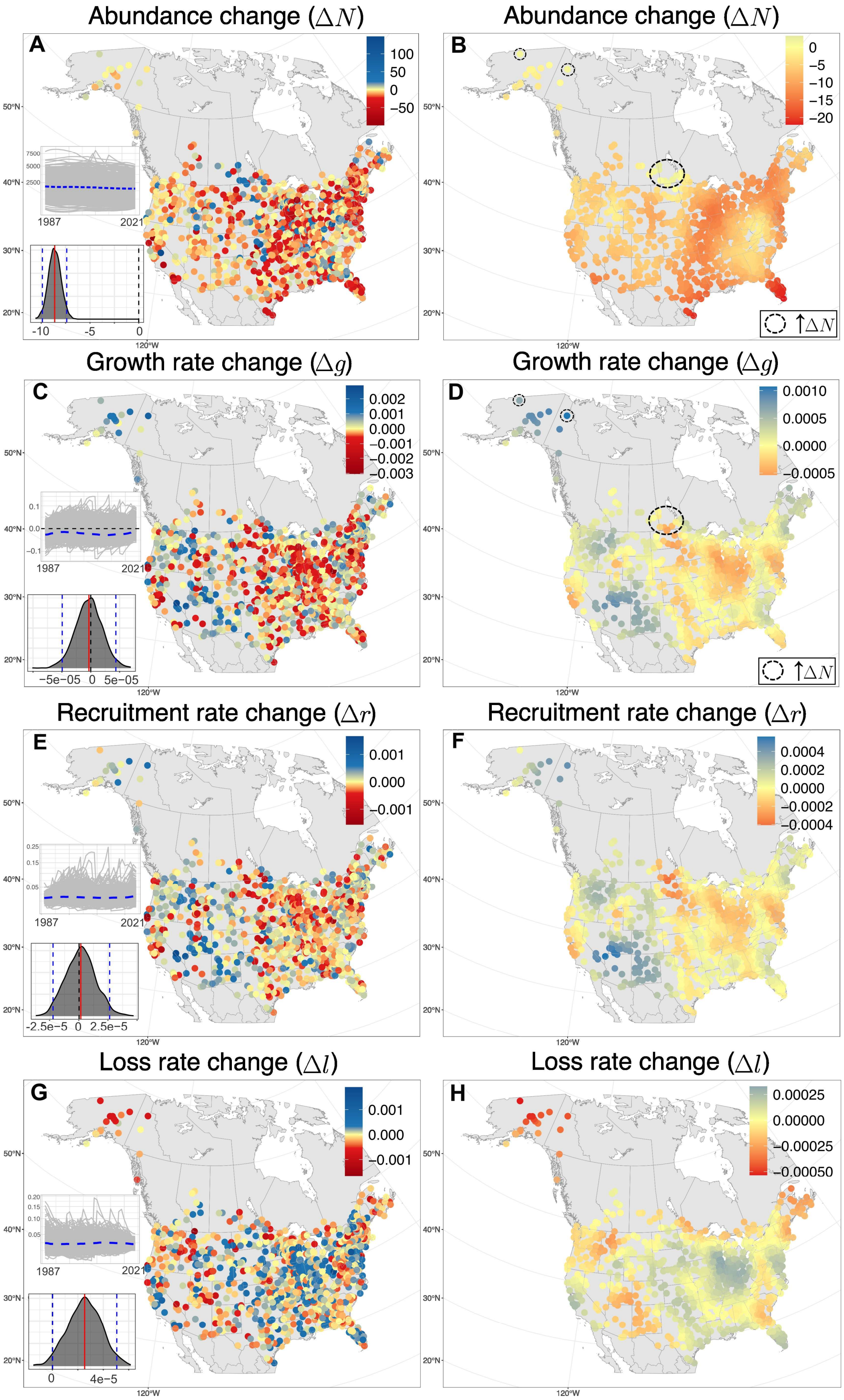
Abundance change (ΔN)
A
100
50
0
−50
7500
5000
2500
1987
2021
-10
-5
0
Abundance change (ΔN)
B
0
−5
−10
−15
−20
$\uparrow \Delta N$
Growth rate change (Δg)
C
0.002
0.001
0.000
−0.001
−0.002
−0.003
0.1
0.0
-0.1
1987
2021
−5e−05
0
5e−05
Growth rate change (Δg)
D
0.0010
0.0005
0.0000
−0.0005
$\uparrow \Delta N$
Recruitment rate change (Δr)
E
0.001
0.000
−0.001
0.25
0.15
0.05
1987
2021
-2.5e−5
0
2.5e−5
Recruitment rate change (Δr)
F
0.0004
0.0002
0.0000
−0.0002
−0.0004
Loss rate change (Δl)
G
0.001
0.000
−0.001
0.20
0.15
0.10
0.05
1987
2021
0
4e−5
Loss rate change (Δl)
H
0.00025
0.00000
−0.00025
−0.00050
50°N
40°N
30°N
20°N
120°W

Fig S1 | (A - B) Total abundance change in bird population from 1987 to 2021 (ΔN), and (C-D) temporal change of yearly growth rate decomposed into (E-F) temporal change of recruitment rate, and (G-H) temporal change of loss rate, after correcting for imperfect detection. Each dot represents random slope of a linear regression between the metric and time for one of the 1,033 routes of the North American Breeding Bird Survey. The left column (A-C-E-G) shows the values of the model output, and the right column (B-D-F-H) the spatially smoothed values using a spatial GAM with a gaussian process smoother. The color palettes of the smoothed maps (right column) have been used for the model outputs maps (left column). Inset plots in bottom left show the raw (i.e. not smoothed) trends in abundance, growth, recruitment, and loss rates in a semi square root space for each BBS route in grey, with the average trend in blue dashed line. The histograms show the posterior distributions of the grand slope with the red vertical line indicating the mean and the dashed blue lines the 95% credible interval.

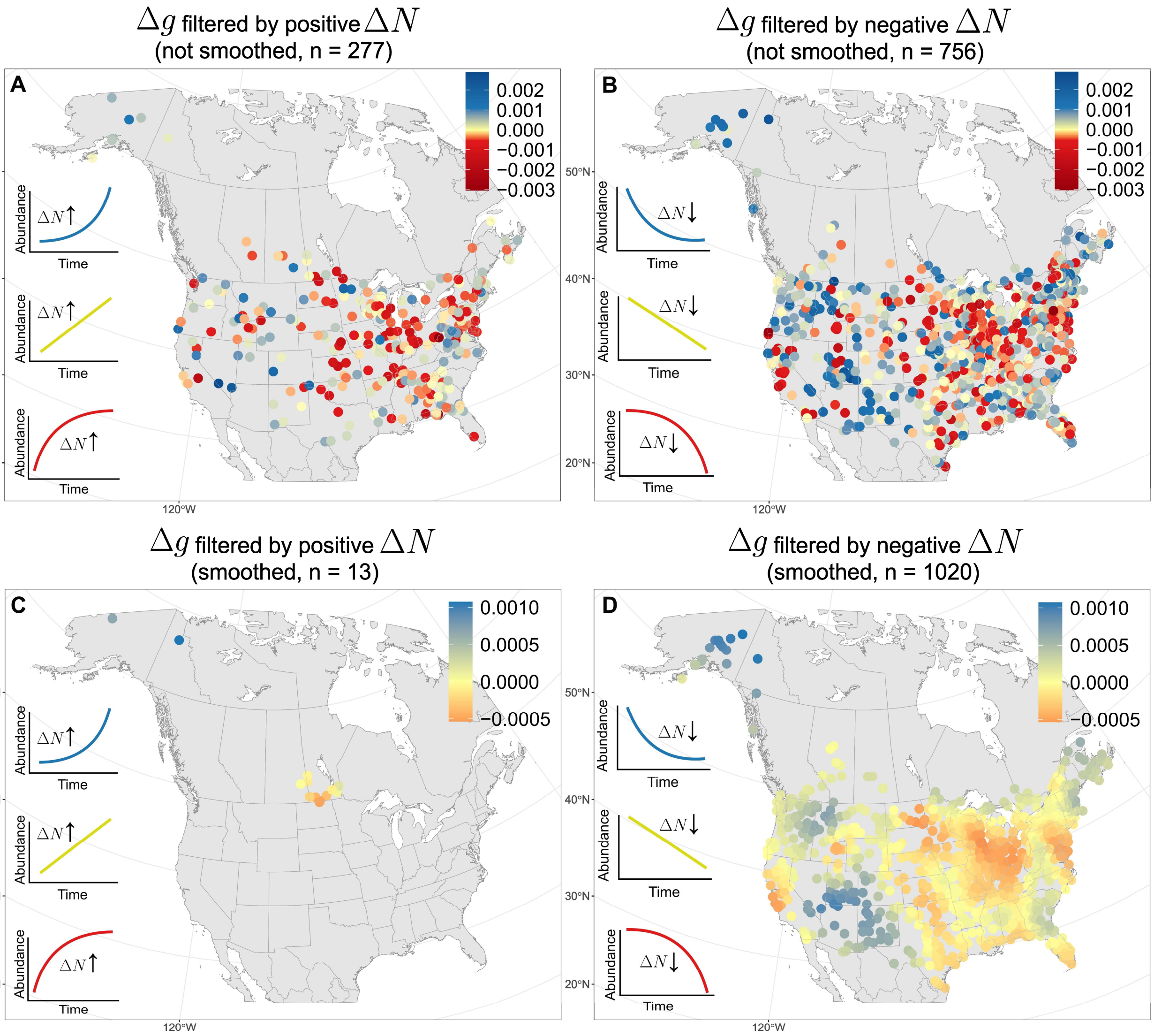

Δg filtered by positive ΔN (not smoothed, n = 277)

Δg filtered by negative ΔN (not smoothed, n = 756)

Δg filtered by positive ΔN (smoothed, n = 13)

Δg filtered by negative ΔN (smoothed, n = 1020)

Fig. S2 | Values of growth rate change (Δg) filtered by positive abundance change ΔN (A-C) or negative ΔN (B-D) for the raw output of the models (A-B), and the spatially smoothed values (C-D). In essence, the left column (A-C) shows maps of the accelerated and decelerated abundance increase, while the right column shows the acceleration and deceleration of the decline. Inset plots show the shape of ΔN according to the values of Δg. The information of these maps has been summarized in Fig. 2A-B by adding the black dotted circles to indicate regions with positive ΔN.

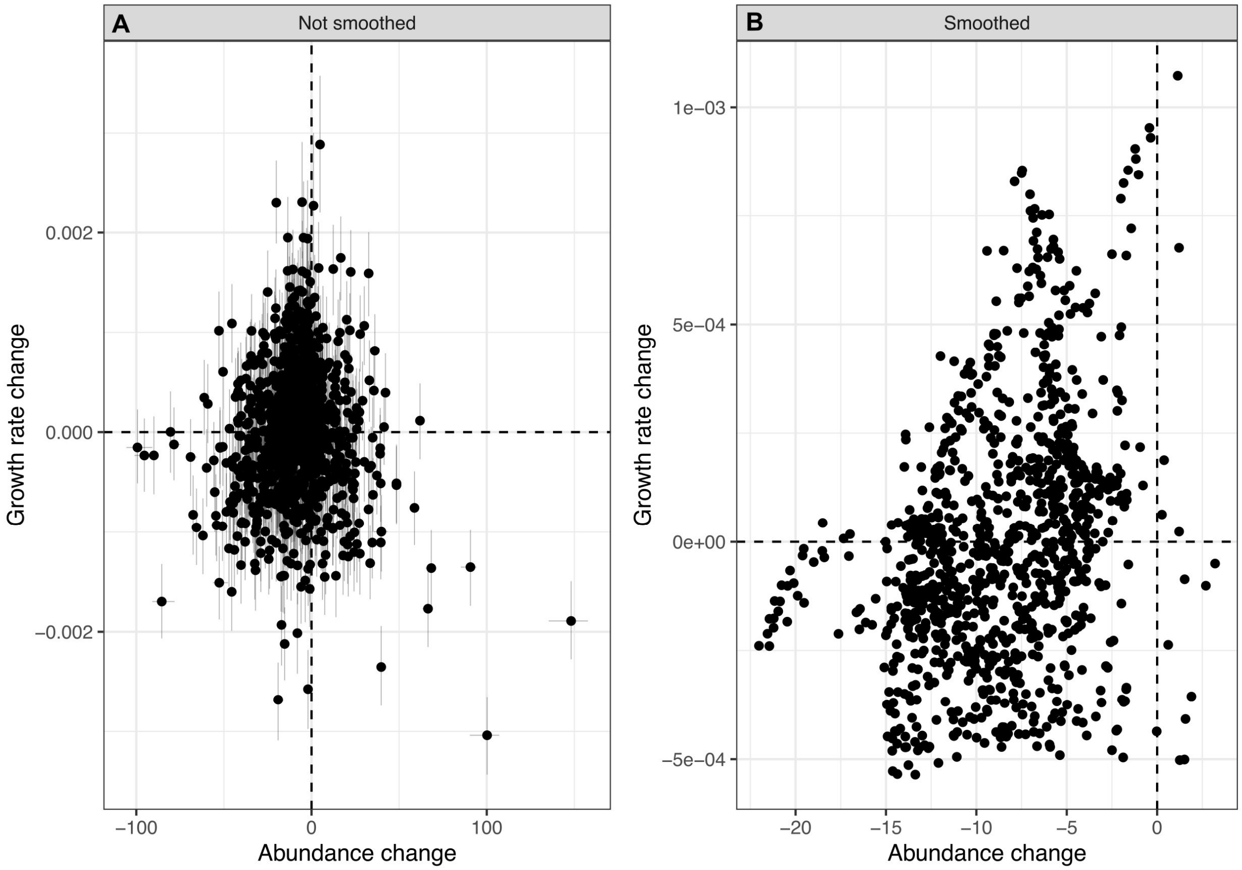

Fig. S3 | Per route values of change in abundance (ΔN) vs. change in growth rate (Δg) for (A) the outputs of the model and (B) the spatially smoothed data. Error bars in (A) show the 95% Credible Interval of the MCMC propagated uncertainty. This representation helps to show the routes with accelerating/decelerating decline/increase of abundance. Note that the scale for panels (A) and (B) are different.

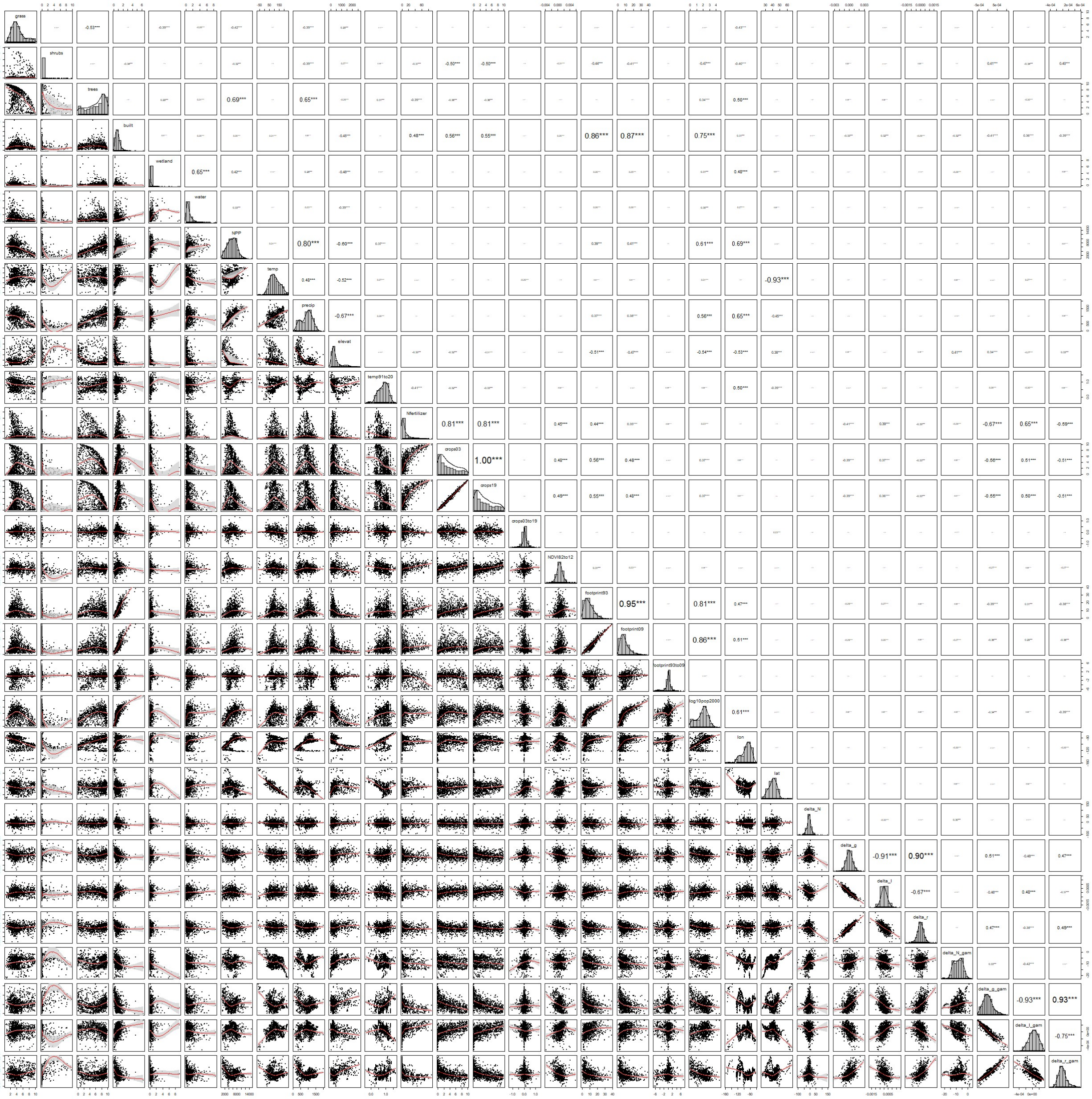

Fig. S4 | Correlations between the environmental and human-related variables, and ΔN, Δg, Δl, Δr (raw outputs and spatially smoothed with a GAM). Numbers in the upper right triangle are Spearman correlation coefficients, with larger values in larger letters. For explanation of variable names and details see Table S1.

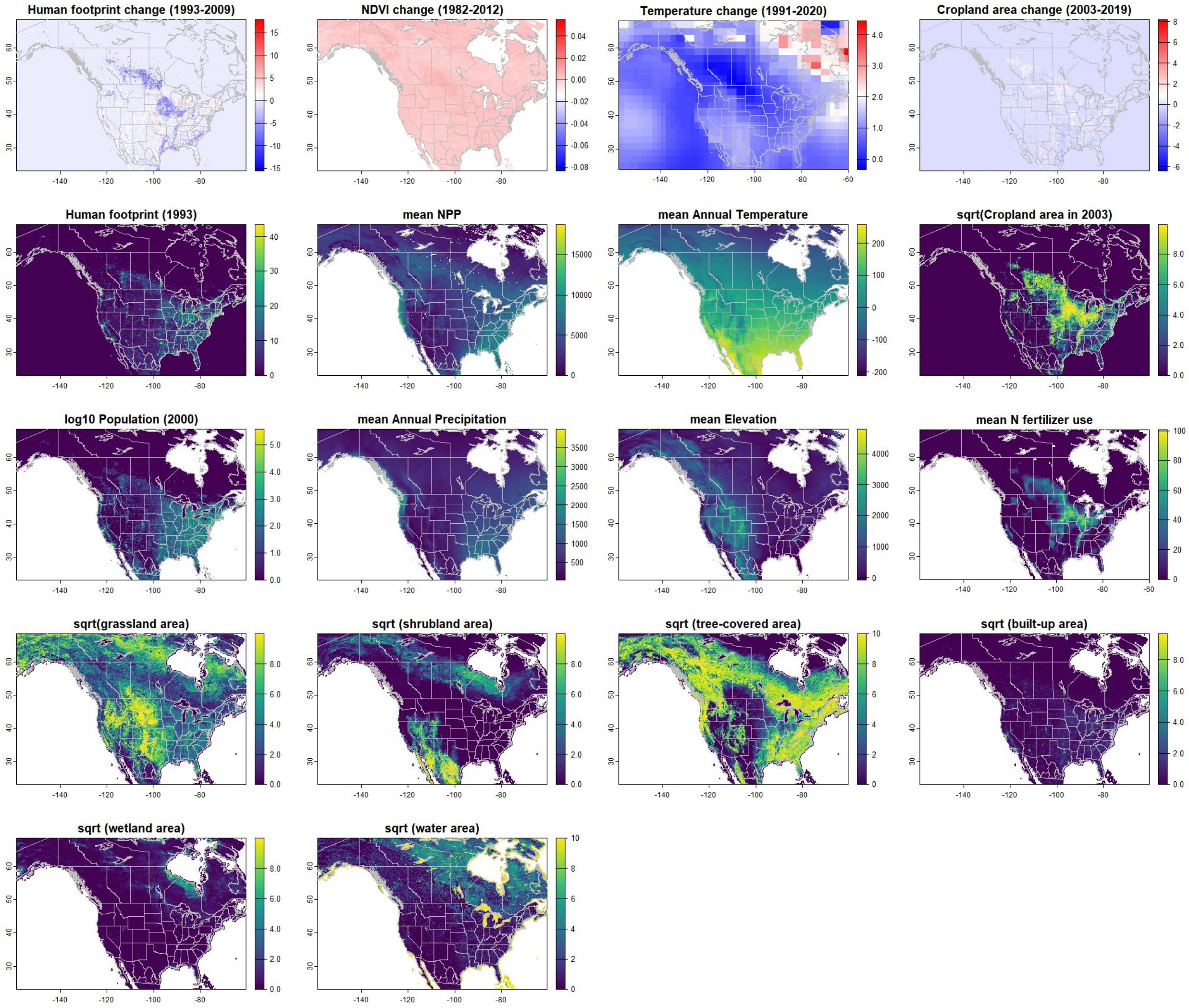

Human footprint change (1993-2009)

NDVI change (1982-2012)

Temperature change (1991-2020)

Cropland area change (2003-2019)

Human footprint (1993)

mean NPP

mean Annual Temperature

sqrt(Cropland area in 2003)

log10 Population (2000)

mean Annual Precipitation

mean Elevation

mean N fertilizer use

sqrt(grassland area)

sqrt (shrubland area)

sqrt (tree-covered area)

sqrt (built-up area)

sqrt (wetland area)

sqrt (water area)

Fig. S5 | Maps of environmental and human-related variables used in the post-hoc analysis. Details on each are in Table S1. Variables in the top row represent temporal change, while the rest of the variables are static averages.

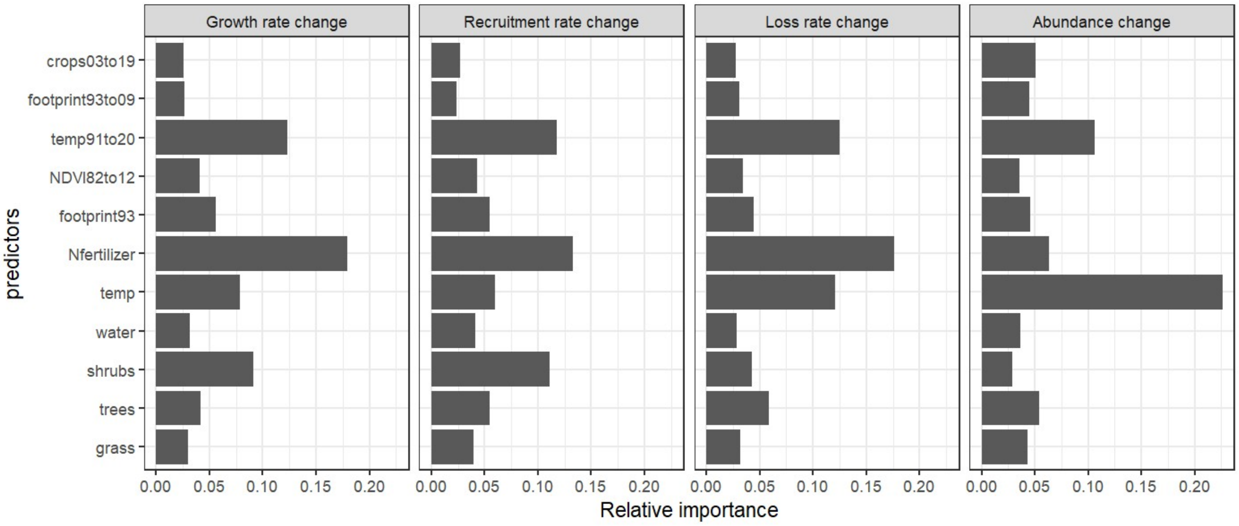

Fig. S6 | Relative variable importances from random forest algorithm explaining changes in growth rate Δg (total var. explained = 72.5%), recruitment rate Δr (total var. explained = 70.8%), loss rate Δl (total var. explained = 71.7%), and abundance ΔN(total var. explained = 74.1%). Details of the covariates are in Table S1. To avoid collinearity, we only used a subset of the variables from Table S1 (see details in Methods). Variable importances are the mean decreases in accuracy over every tree in the forest while permuting the Out Of Bag data. These were then scaled to relative importances, so that they add up to the total percentage of explained variance by a given random forest.

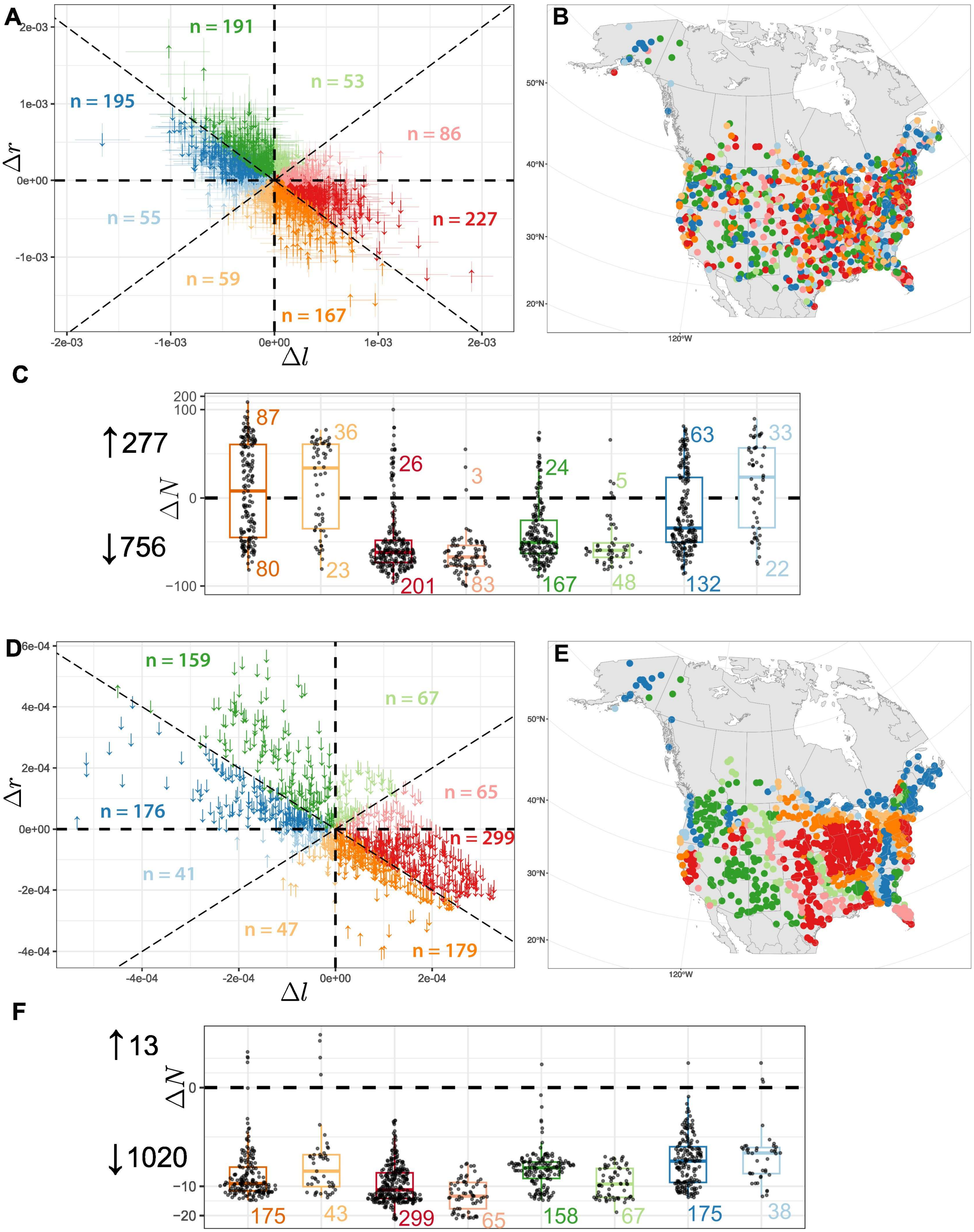

Fig. S7 | (A-D) Predicted growth rate change (Δg) projected in a loss rate change (Δl) – recruitment rate change (Δr) space for (A) raw outputs of the models and (D) spatially smoothed values. Arrows (↑ and ↓) indicate abundance increases and declines (respectively), for each

Breeding Bird Survey route. Colors represent whether the dominant process of Δg is due to negative Δl (blue), positive Δr (green), negative Δr (orange) or positive Δl (red) (see Fig. 1 for details). Error bars in (A) show the 95% credible interval of the propagated uncertainty. (B-E) Maps of Δg values that fall within each category of the Δr – Δl space for (B) the raw outputs of the models and (E) the spatially smoothed values. (C-F) Distributions of increasing and decreasing populations ΔN falling within each $\Delta l \Delta r$ class for the 1033 BBS routes in our analysis for (C) the raw outputs, and (F) the spatially smoothed values.

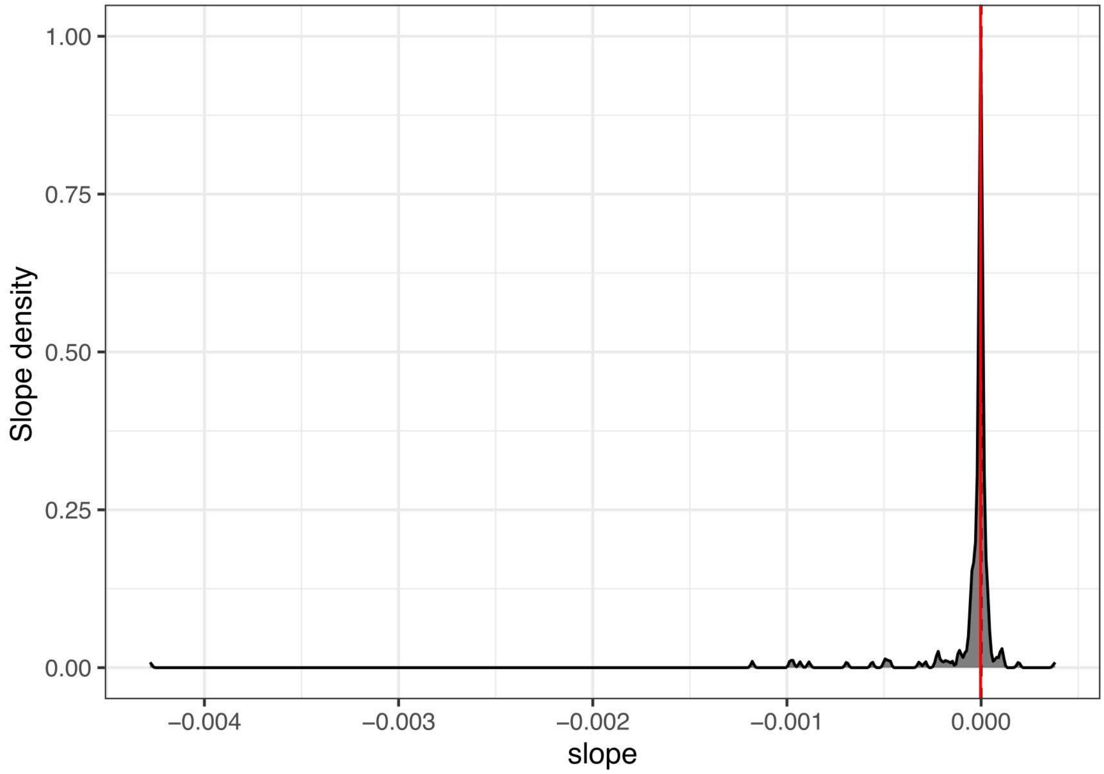

Fig. S8 | Density distribution of the slopes between growth rate and abundance (i.e. density dependence relationship) for all 234 species in our analysis. The median slope is the red vertical line; it falls close to 0, indicating that there are approximately as many positive as negative density dependent relationships.

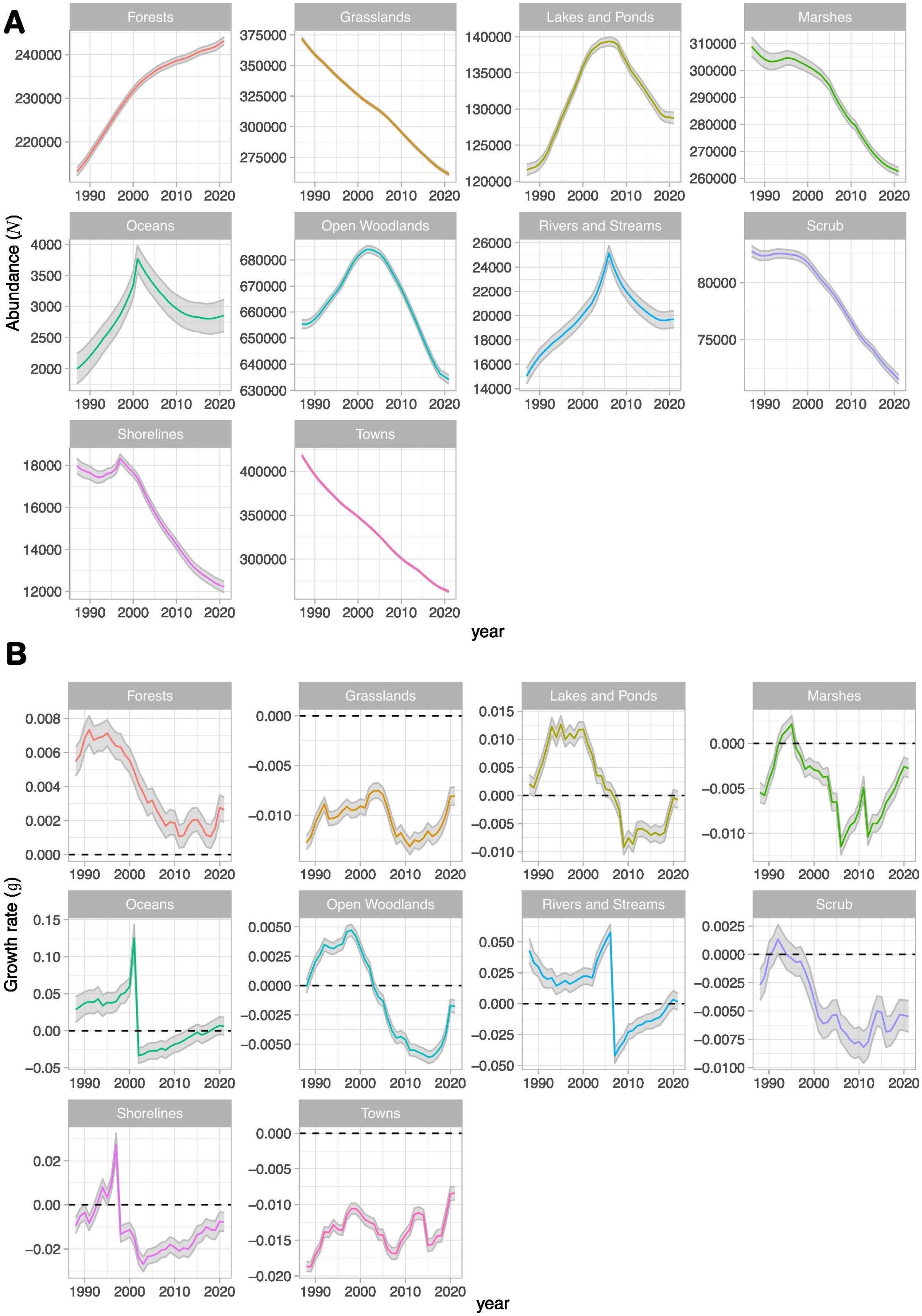

Fig. S9 | Temporal changes in (A) abundance ΔN, and (B) growth rate Δg for different bird preferred habitat types. The grey areas show the propagated 95% credible interval of the MCMC chains.

Table S1 | Details of variables used in the post-hoc correlative analysis of patterns of change and acceleration. We downloaded each variable as a spatial raster in its *original resolution* and aggregated it to the *coarsened resolution*. The aggregation function was either sum (for areas of land cover classes and cropland area) or mean (for the rest of variables). When the original and analyzed resolution are identical in the table, no aggregation was done. We then overlaid each BBS route over the coarsened raster, and we calculated the mean value of all pixels overlapping the route.

Abbreviation	**Variable**	**Coarsened resolution (original resolution)**	**Citation**	**Available from**
grass, shrubs, trees, built, wetland, water	Area of land cover classes (in 2020), square root transformed	5 min (30 sec)	(*48*)	"geodata" package in R
NPP	Mean MODIS-derived Net Primary Productivity (MOD17A3 product, 2000-2015)	5 min (500 m)	(*49*)	https://lpdaac.usgs.gov/products/mod17a3hgfv061/ (downloaded by Petr Keil in 2019)
temp	Mean annual temperature (1970-2000)	5 min (30 sec)	(*50*)	www.worldclim.org
precip	Mean annual precipitation (1970-2000)	5 min (30 sec)	(*50*)	www.worldclim.org
elevat	Elevation above sea level	5 min (30 sec)	(*51*)	"geodata" package in R or https://srtm.csi.cgiar.org
temp87to21	Trend of mean annual temperature between 1987 and 2021 (GHCNv4 dataset, smoothing radius 250 km)	2° (2°)	(*52*, *53*)	https://data.giss.nasa.gov/gistemp/maps/
Nfertilizer	Nitrogen fertilizer use (1994-2001)	0.5° (0.5°)	(*54*)	https://search.earthdata.nasa.gov/
crops03	Cropland area in 2003, square root transformed	5 min (30 sec)	(*25*)	"geodata" package in R or https://glad.umd.edu/dataset/croplands
crops03to19	Difference of square root of cropland area between 2003 and 2019	5 min (30 sec)	(*25*)	"geodata" package in R or https://glad.umd.edu/dataset/croplands
NDVI82to12	Trend in normalized difference vegetation index (NDVI) between 1982 and 2012	0.08° (0.08°)	(*55*)	https://webmap.ornl.gov/ogc/dataset.jsp?ds_id=1275
footprint93	Human footprint index in 1993	5 min (30 sec)	(*56*)	"geodata" package in R or https://datadryad.org/stash/dataset/doi:10.5061/dryad.052q5
footprint93to09	Difference of human footprint index between 1993 and 2009	5 min (30 sec)	(*56*)	"geodata" package in R or https://datadryad.org/stash/dataset/doi:10.5061/dryad.052q5
pop2000	Human population density in 2000, $\log_{10}(x+1)$ transformed	5 min (30 sec)	(*57*)	https://cmr.earthdata.nasa.gov/search/concepts/C1597158029-SEDAC.html